RESEARCH ARTICLE

A Fast and Scalable Kymograph Alignment Algorithm for Nanochannel-Based Optical DNA Mappings

Charleston Noble[1,2¤], **Adam N. Nilsson**[1], **Camilla Freitag**[2,3], **Jason P. Beech**[2], **Jonas O. Tegenfeldt**[2], **Tobias Ambjörnsson**[1]*

1 Department of Astronomy and Theoretical Physics, Lund University, Lund, Sweden, **2** Division of Solid State Physics, Department of Physics, Lund University, Lund, Sweden, **3** Department of Physics, Gothenburg University, Gothenburg, Sweden

¤ Current address: Department of Systems Biology, Harvard Medical School, Boston, MA 02115, USA
* tobias.ambjornsson@thep.lu.se

OPEN ACCESS

Citation: Noble C, Nilsson AN, Freitag C, Beech JP, Tegenfeldt JO, Ambjörnsson T (2015) A Fast and Scalable Kymograph Alignment Algorithm for Nanochannel-Based Optical DNA Mappings. PLoS ONE 10(4): e0121905. doi:10.1371/journal.pone.0121905

Academic Editor: Mark Isalan, Imperial College London, UNITED KINGDOM

Received: October 1, 2014

Accepted: February 5, 2015

Published: April 13, 2015

Data Availability Statement: All relevant data are within the manuscript and on Figshare via http://dx.doi.org/10.6084/m9.figshare.1312910.

Funding: TA, Swedish Research Council, grant no. 2009-2924, http://www.vr.se/ Funding provided to JOT, 2007-584, Swedish Research Council, grant no. 2007-584, http://www.vr.se/, JOT, VINNOVA, grant number P35735-1, http://www.vinnova.se/en/, TA, The Carl Tryggers Foundation grant no. 12:13 http://www.carltryggersstiftelse.se/, and JOT, The Hasselblad Foundation http://www.hasselbladfoundation.org/news. The funders had no

Abstract

Optical mapping by direct visualization of individual DNA molecules, stretched in nanochannels with sequence-specific fluorescent labeling, represents a promising tool for disease diagnostics and genomics. An important challenge for this technique is thermal motion of the DNA as it undergoes imaging; this blurs fluorescent patterns along the DNA and results in information loss. Correcting for this effect (a process referred to as kymograph alignment) is a common preprocessing step in nanochannel-based optical mapping workflows, and we present here a highly efficient algorithm to accomplish this via pattern recognition. We compare our method with the one previous approach, and we find that our method is orders of magnitude faster while producing data of similar quality. We demonstrate proof of principle of our approach on experimental data consisting of melt mapped bacteriophage DNA.

Introduction

Optical mapping is an emergent complementary approach to DNA sequencing which produces a lower resolution (typically kbp) sequence-dependent map of individual DNA molecules [1–10]. As a direct complement to DNA sequencing, optical mapping can produce a scaffold to facilitate easier sequence assembly, and as an indirect complement, optical mapping promises a variety of applications for which low resolution maps will suffice. For example, it can be used to quickly identify large-scale structural variations, including duplications, deletions, insertions, inversions, and translocations, which are increasingly being linked to heritable traits of phenotypic significance [3, 11, 12], and it allows for the rapid identification of bacterial species and strains which could represent an important step against the growing problem of antibiotic resistance [13–17].

To date, many techniques for optical mapping have been developed, and they typically rely on sequence-specific DNA modifications at short target sites, followed by imaging and analysis. These sequence-specific modifications can include staining and denaturation ("melt mapping")

role in study design, data collection and analysis, decision to publish, or preparation of the manuscript.

Competing Interests: The authors have declared that no competing interests exist.

[18], fluorocoding [19], competitive binding of intercalating dyes [20, 21], methylation [22], enzymatic nicking [23, 24], and enzymatic restriction [25–27].

These optical mapping techniques can roughly be divided into three groups: stretching over a surface [9, 28–30], stretching via confinement in nanochannels [4, 31–36] or stretching via elongational flow in microchannels [37]. While surface–stretching techniques offer a few advantages, such as allowing for 100–140% extension [26], mapping via nanochannel confinement allows for integration of the stretching in a lab on a chip context that in turn can be brought to application much more easily.

Note that the nanochannel-based DNA barcoding schemes, the main focus of this study, should not be confused with schemes where short genetic markers [38] or restriction enzyme cleavage events [25] are detected as landmarks. Barcodes addressed by our technique are not simply binary in the sense that one detects landmarks or the absence thereof; rather what we call "barcodes" are continuous fluorescence profiles which are more susceptible to thermal noise (see Fig 1a).

One particular problem inherent to nanochannel confinement techniques is that DNA tends to undergo random diffusive processes during imaging, including center-of-mass diffusion and local stretching [39]. To correct for these effects, a procedure we denote *kymograph alignment* must be performed (see section Problem Definition). In this paper we present WPAlign (**W**eighted **P**ath **Align**), an algorithm for kymograph alignment which offers linear scaling in time and can align DNA barcodes with length corresponding to an entire human genome in less than an hour on a typical desktop computer. We compare its performance to an existing technique and show that our method offers orders-of-magnitude improvement in computational speed while producing processed data of similar quality. Additionally, we present a new information score which quantifies the information content of DNA barcodes and should see widespread use as a barcode quality criterion by which experimentalists can evaluate barcodes and optimize experimental mapping conditions.

Problem Definition

In Fig 1a, the result of a typical nanochannel-based optical DNA mapping experiment is displayed. The horizontal axis (x-axis) of this kymograph represents the DNA's extension in the nanochannel (where the pattern results from sequence-specific staining), and the vertical (y-axis) represents images of the DNA molecule at different times.

Due to thermal center of mass and local conformational fluctuations (which occur because the flexible DNA molecule is only extended to roughly 50 percent of its contour length), the images over time are misaligned both locally and at a global level, leading to significant noise during time-averaging (see Fig 1c). Thus before a useful time-average can be performed, the bright and dark bands must be "straightened"; this procedure we refer to as *kymograph alignment*. Fig 1b shows the result of our algorithm, WPAlign, developed for this particular task, and Fig 1d shows the corresponding time-average. The details of the algorithm can be found in the Methods section. Intuitively, the purpose of this process is to, as closely as possible, mimic the results which would be obtained if the DNA were held and stretched to 100 percent of its length during imaging. For practical experimental reasons, this is not feasible for nanochannel-based techniques, so one must correct for misalignments such as those displayed in Fig 1a.

In Ref. [18], the kymograph alignment challenge is mathematically presented as a global optimization problem (see S1 for details): a template time frame, T, is first chosen. One then allows for local stretching of all the remaining frames, N_i, and maximizes the overlap between N_i and T. Finally, all the time frames are rescaled with average global stretching factors in order to

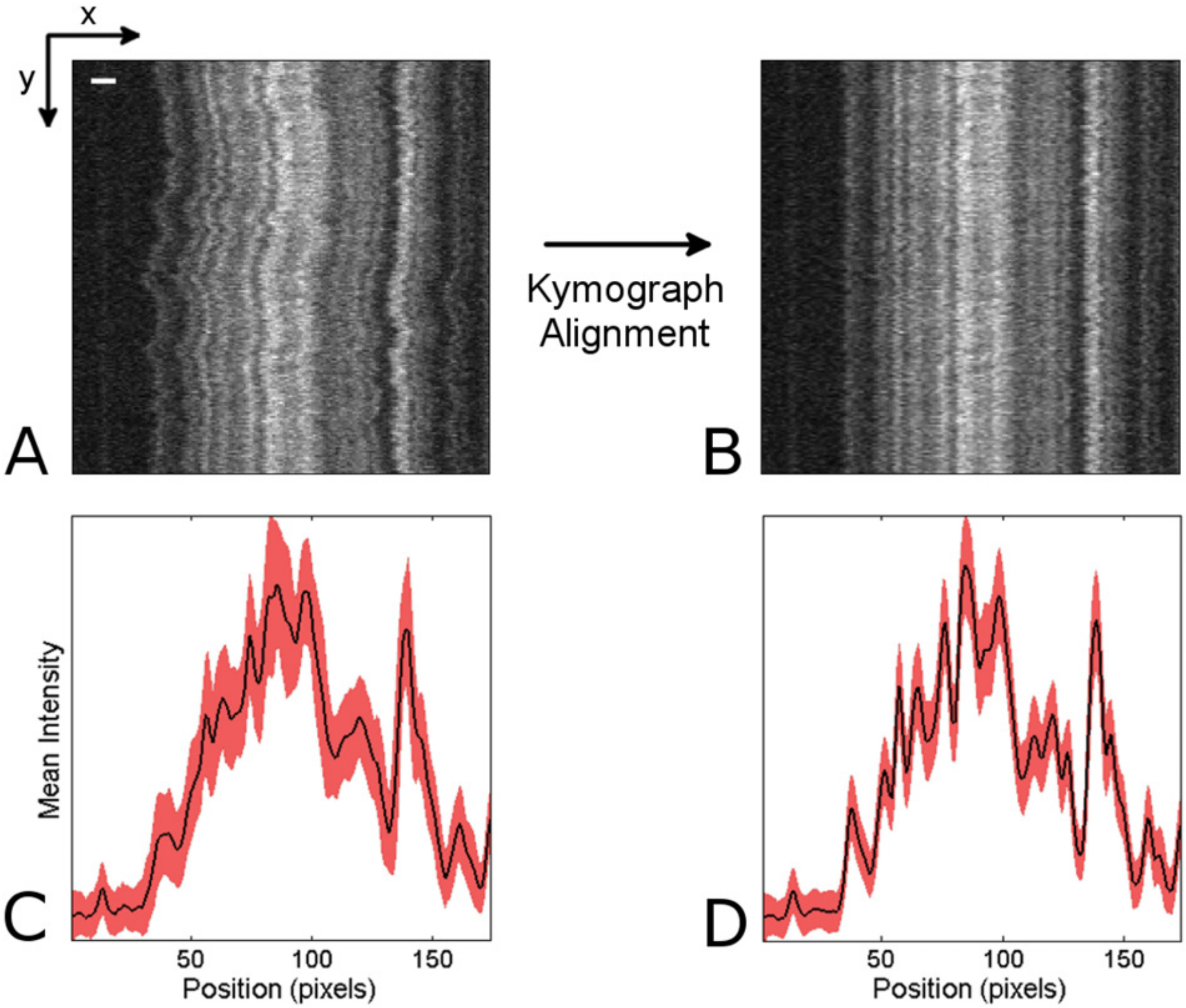

Fig 1. Problem definition. (A) A raw kymograph depicting denaturation mapping of an intact T4GT7 bacteriophage DNA molecule. The y-axis represents time (200 time frames over 20 seconds) while the x-axis represents the DNA extension in the nanochannel (170 pixels wide; scale bar is 2μm). Note that these specifications also apply to all of the following kymographs. (B) The image from (A) after undergoing the kymograph alignment process. (C) Trace of mean intensity over time for the raw kymograph (black) with ±1 standard deviation (red), and (D) the same for the aligned kymograph.

doi:10.1371/journal.pone.0121905.g001

ensure that the end-to-end distance of the DNA molecule after alignment is unchanged and that the time-averaged optical map is therefore consistent with thermodynamic constraints.

In this study we pose the kymograph alignment challenge in slightly different mathematical terms, namely as a feature detection problem (details found in Methods). Visually, our method (see Results) produces appealing images which are very similar to those produced using the previous method. The main benefit of our approach is that it provides an orders-of-magnitude reduction in computational time. Furthermore, all the substeps in our algorithm use standard numerical tools and are, therefore, straightforward to implement.

The rest of this study is organized as follows: in Methods we introduce our kymograph alignment algorithm, WPAlign. In Results, we compare our new algorithm to the previous method. In Discussion we summarize our results and point to further potential applications of our algorithm, and in the S1 we provide more technical details of our approach.

Methods

We now consider the problem defined in the previous section, i.e., the alignment of a "fuzzy" DNA barcode (see Fig 1a for an illustrative example) distorted by thermal fluctuations as it resides in a nanochannel. WPAlign works intuitively by detecting pronounced bright or dark ridges ("features") and then stretching the barcode horizontally to straighten them. The advantage of this approach is that it reduces the problem to a simple two-step process of (1) *single-feature detection*, followed by (2) *single feature alignment*. This two-step process is then be applied recursively to align the entire kymograph.

Single Feature Detection

Consider an image represented as a 2D gray scale intensity function with columns x and rows y, denoted $I(x, y)$, $x \in [1, n]$, $y \in [1, m]$. See Fig 1a for an illustrative example. Then a feature $x = F(y)$ is a function mapping of rows Y to columns X. This mapping thus provides a curve, $(x, y) = (F(y), y)$, through the image. Intuitively the feature F we would like to detect is the "most pronounced" vertical ridge or valley in I such that:

1. (Completeness) Our detected feature F traverses each row y exactly once. Actual features might not adhere to this constraint, since anomalous events such as DNA breakage could occur, but these events should be treated separately from the alignment process.
2. (Continuity) F's horizontal movement is constrained. I.e., $|F(y{+}1) - F(y)| \leq k$ for some integer k and for all y. This is to fit the physical constraints we inherit from the polymer physics of DNA molecules for the present application.

Unfortunately, standard feature detection (e.g., ridge detection) methods cannot be applied directly, as the resulting features will not necessarily satisfy these constraints, so we have developed the following three-step procedure for *single feature detection*:

1. Image pre-processing. First the entire image is smoothed with a 2D Gaussian kernel (here we use $\sigma_h = 10$ pixels and $\sigma_v = 3$ pixels, where h and v represent the horizontal and vertical directions, respectively) to remove noise from random intensity fluctuations (see Fig 2b). Then we apply a Laplacian of Gaussian filter to obtain the *Laplacian response* image which we refer to as K (see Fig 2c), a matrix with the same size as I which has large positive values in dark bands and large negative values in light bands (see also S1). These positive and negative values are linearly rescaled to range from (0,1] and [−1,0), respectively.

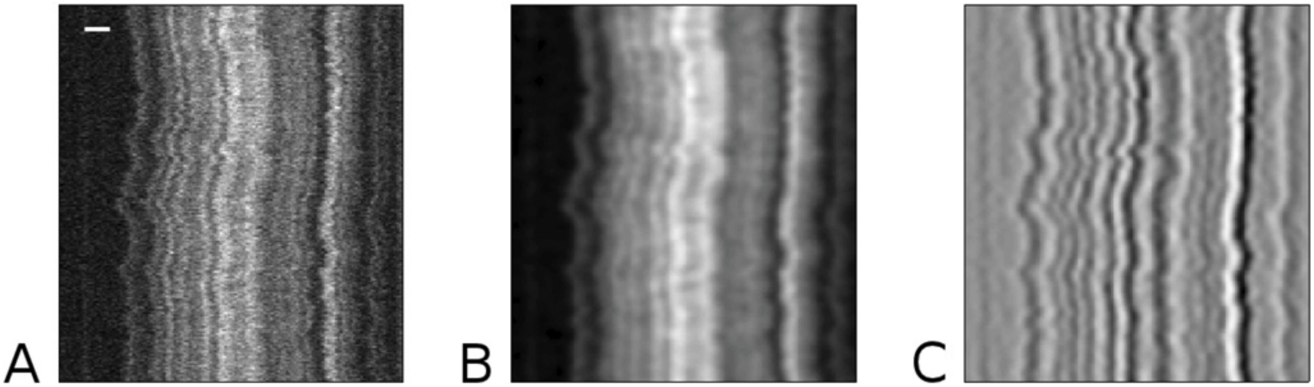

Fig 2. Image preprocessing. (A) The raw, unaligned, kymograph shown in Fig 1a (scale bar is 2 μm, 20 seconds of imaging). (B) The kymograph after Gaussian smoothing, and (C) The Laplacian response image, which we refer to as K, that results from applying the Laplacian of Gaussian filter (with $\sigma = 10$ pixels) to our smoothed kymograph. In K, dark regions represent positive values and light regions represent negative values.

doi:10.1371/journal.pone.0121905.g002

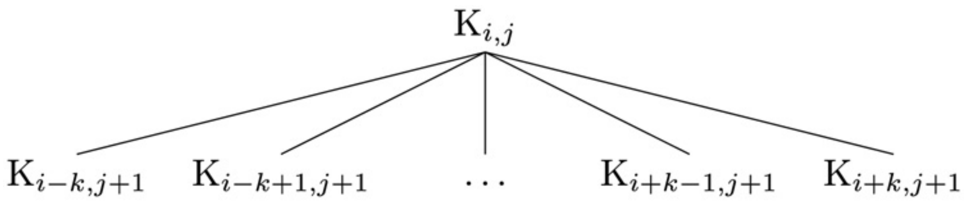

Fig 3. Connectivity between nodes.

doi:10.1371/journal.pone.0121905.g003

Now our feature F should be represented by a continuous region of high (valley) or low (ridge) values in K. We would like to treat these as two distinct cases to avoid detecting a single feature which is partially composed of a ridge and partially composed of a valley, so we compute two separate images, K_B and K_D which emphasize bright and dark regions, respectively (see Fig 3, Fig 4 and S1). Both are positive or zero everywhere, with the smallest values representing the most pronounced feature locations.

2. Network assembly. We can think of the images K_B and K_D as energy landscapes, and finding the best ridge or valley becomes a problem of finding the lowest-energy paths through K_B and K_D, respectively. To do this, we assemble directed, acyclic networks G_B and G_D as follows (see Fig 4). For simplicity, we describe our process only for G_B, as the process is identical for G_D.

1. First, we create one node for every pixel in K_B, plus two “peripheral” nodes. Thus G_B consists of $(m \times n+2)$ nodes.

2. Now the first of the peripheral nodes is connected to each of the nodes corresponding to the first row of G_B, and each of the last-row nodes is connected to the second peripheral node with edge weight 1.

3. The rest of the nodes are connected as follows: the node corresponding to pixel (i, j) in K_B is connected to pixels in the next row directly below, to the left k columns, and to the right k columns (see Fig 3). This k value is used to satisfy the continuity constraint above. We have found $k = 2$ to be reasonable for our current application.

4. If a pixel is too close to a border on the left or right (i.e., $i - k < 1$ or $i+k > n$), connections to non-existing nodes prescribed in step 3 are ignored.

5. Finally, every edge is assigned a weight equal to the intensity of the pixel in K_B corresponding to the node it is directed to.

Note that the edge weights in this connection scheme are not “biased,” in the sense that given equal intensities, movement to any of the connected pixels is equally likely. Alternatively, one could assign a non-uniform distribution such that the edge weights are given by a combination of intensities and some prior knowledge of likely fluctuations. For example, the weight of the edge connecting (i, j) to (i', j') could be given by $w_{i \to i', j \to j'} = I(i', j')f(i', i)$, where f is some probability distribution. Our scheme here represents a special uniform case where $f(i', i) = 1/(2k + 1)$ for $|i' - i| \leq k$ and $f(i', i) = 0$ otherwise.

After examining several additional forms for f, we found that the simple uniform case presented above achieved the best and most consistent results for our examples. However, this weighting scheme should, in general, be carefully chosen by the user to suit the particular data being considered.

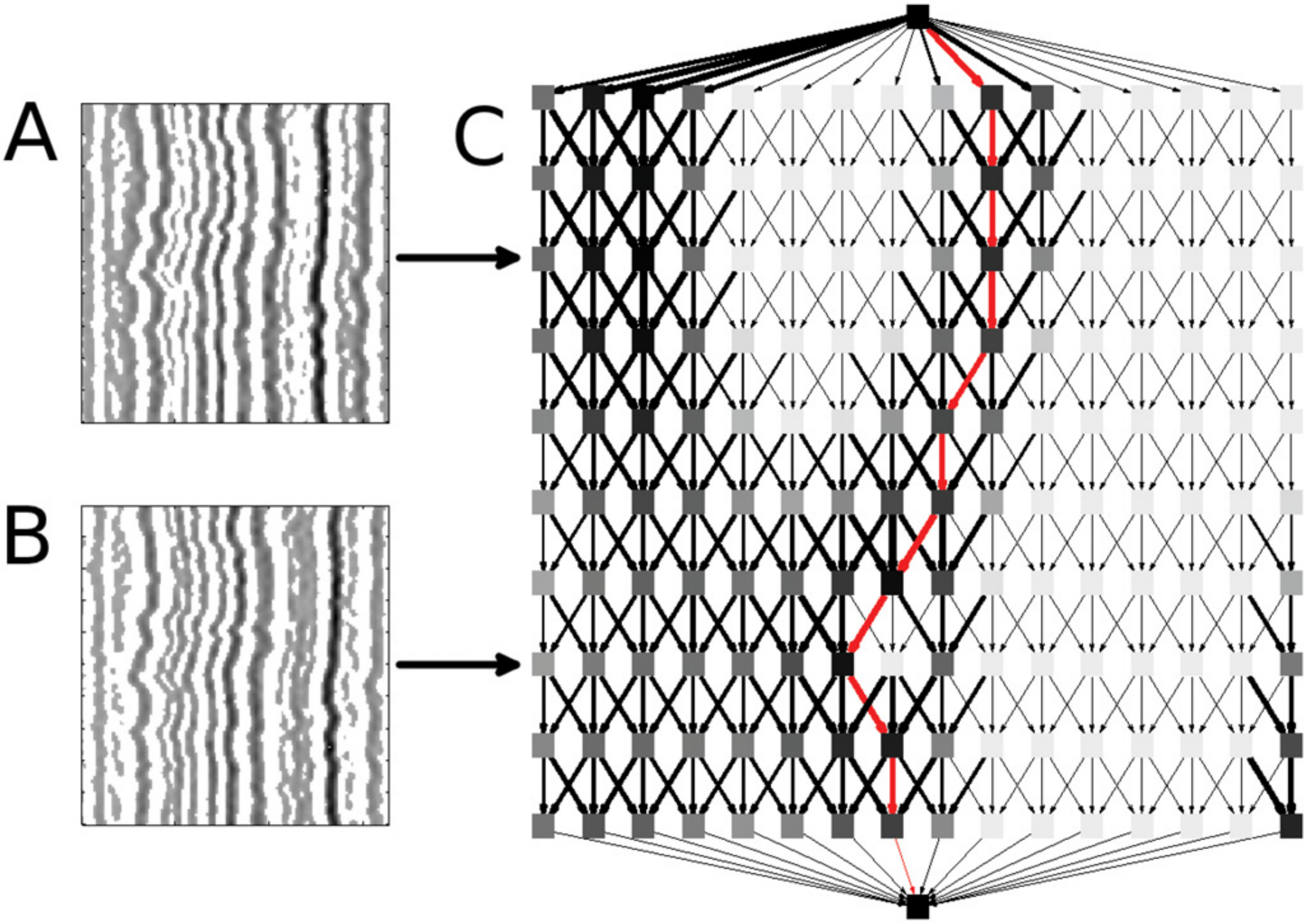

Fig 4. Network assembly. The Laplacian response image, K, (see Fig 2c) has been rescaled into (A) K_D and (B) K_B, images that emphasize dark and bright regions in K, respectively. White pixels represent barriers that potential features cannot cross, while continuous dark regions indicate likely features. (C) Here we show one example network, although separate networks are indeed assembled for K_B and K_D. Each node (square) within the rectangular region represents a pixel in K_B or K_D. The top and bottom nodes (which we term "peripheral nodes") are added to provide starting/ending points for the shortest path finding algorithm. The width of the edges corresponds to the inverse of the edge weight, and the darkness of the nodes represents the average weight of incoming edges. The red line illustrates the shortest path through the network. For the sake of visual clarity, this network was created using a small subsection of an actual Laplacian response with $k = 1$.

doi:10.1371/journal.pone.0121905.g004

As for the choice of k, we found $k = 2$ to be reasonable for the data presented here; now we present a method for choosing k to be used on novel data. For unbiased diffusive motion, the diffusion length ΔL of the DNA molecule is connected to time as $\Delta L^2 \propto Dt$ (where t is the inverse sampling frequency), and the center-of-mass diffusion constant D is inversely proportional to the number of polymer segments (i.e., the length of the polymer)[40]. Hence $\Delta L \propto 1/\sqrt{L}$, where L is the length of the DNA molecule. For experimental setups identical to ours, the choice of k will vary based on the DNA length to be aligned according to:

$$k = k_{\text{ref}}\sqrt{\frac{L_{\text{ref}}}{L}}$$

where $k_{\text{ref}} = 2$, as presented here, and $L_{\text{ref}} = 24\mu m$, the length of the molecules presented above.

3. Shortest path finding. Now every path between the peripheral nodes in our networks represents a potential feature which satisfies the continuity and completeness constraints above, so our task is to find the "best" such feature. Essentially, we are searching over all paths between the peripheral nodes which do not move more than k pixels horizontally between any adjacent rows. Our cost function is the sum of pixel intensities over a path, and we seek to minimize this over the space of these acceptable paths. Thus, intuitively, the best bright feature corresponds to the shortest path in K_B, and the best dark feature corresponds to the shortest path in K_D. So, our task becomes a shortest path finding problem.

Since our networks are directed and acyclic, the shortest path can be computed by a standard dynamic programming algorithm based on topological sorting which grows linearly with the sum of the number of edges and nodes [41]. Note that, in our graph, this sum grows bilinearly with the number of time frames and the horizontal width of our input kymographs. And since the number of time frames does not change, in practice, the sum of nodes and edges in our graph grows linearly with the kymograph width. Thus the computational time of the shortest path finding algorithm also grows linearly with the kymograph width.

By this process we obtain two paths, one in K_B corresponding to the best bright feature in our original kymograph, and one in K_D corresponding to the best dark feature. The path with the shorter length of these two is chosen as the best overall feature (see Fig 4). If this feature is distinct enough (i.e., its length is lower than some threshold; see Methods on calculating K_D and K_B) then we proceed with alignment. Otherwise the path is rejected, and recursion is terminated. This can happen, for instance, in large dark 'gaps' associated with low labeling density mapping approaches.

Single Feature Alignment

Once the best feature $F(y)$ has been detected by the three-step process above, it is aligned by setting $F(y) = \langle F(y) \rangle$, where $\langle . \rangle$ denotes the mean (rounding to the nearest integer) for all rows y, and the pixels to the left and right of $F(y)$ are stretched (or compressed) linearly. To determine intensity values at non-integer positions during this linear stretching, we used cubic spline interpolation (see Fig 5). Note that by setting $F(y) = \langle F(y) \rangle$, we ensure that the feature is aligned over its position at thermodynamic equilibrium.

Full Kymograph Alignment

Using the scheme above, the best feature in the input image has been both (1) *detected* and (2) *aligned*. But we wish to detect and straighten all of the features. Thus to continue the process, the image is split vertically along the newly aligned feature (see Fig 5c–5e), and w columns (where w is set to half the width of a typical feature) are removed from each on the side adjacent to the split. Then the (1) *single feature detection* and (2) *single feature alignment* routines are called again on each of these two smaller images if they are wider than typical a feature (i.e., $2w$). In our current application, features are typically $\sim$ 10 pixels wide, so we use $w = 5$ pixels, though this parameter can easily be changed depending on the application. (see Fig 5). The algorithm then terminates when the width of the image is less than the width of a typical feature, $2w$.

It is worth noting that, since we remove columns before calling the process again, the algorithm is guaranteed to converge. If we did not perform this step, the same feature could conceivably be re-straightened perpetually.

A pseudocode describing all the steps in our kymograph alignment method, WPAlign, is found in Fig 6.

Results

In practice, WPAlign produces alignments which are visually appealing (see Fig 7). To quantify the quality of these alignments, we use two quality criteria: *time-trace noise reduction* and

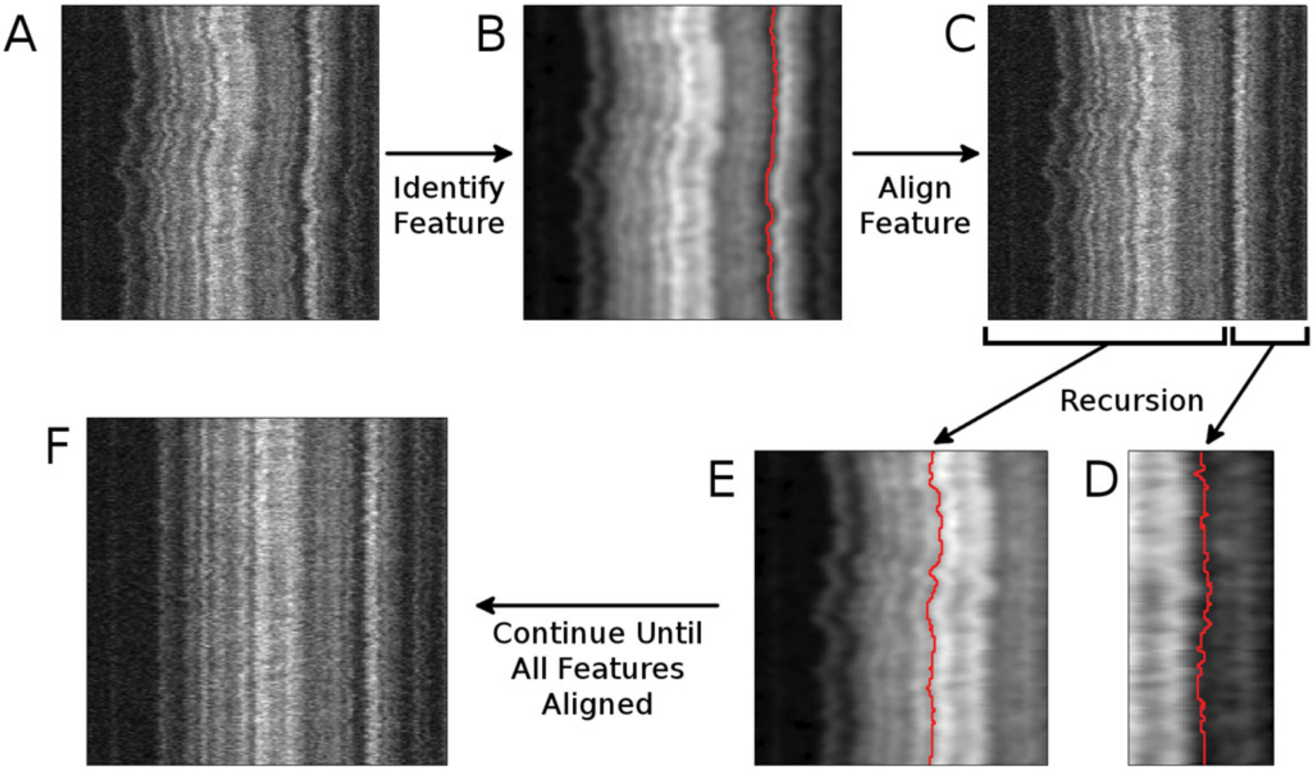

Fig 5. Feature detection and recursion in WPAlign. (A) A raw, unaligned kymograph is given as input (see Fig 1). (B) The "best" feature is identified from the input kymograph. (C) The feature identified in (B) is aligned via linear interpolation. (D, E) The feature identification process is called recursively on the regions to the right (D) and to the left (E) of the newly-aligned feature. (F) This process is continued until all features have been aligned.

doi:10.1371/journal.pone.0121905.g005

information content along with empirical computational costs. We compare WPAlign to the method used in [18] (see S1 for a description) with respect to these measures.

Time Trace Noise Reduction

The ultimate goal of presenting the data in a kymograph format is to produce a 1-dimensional intensity profile that is "typical" and reproducible for the DNA being analyzed. This intensity profile is then compared to existing databases for genomic analysis. To produce this intensity profile, $\langle I \rangle$, we simply take the time-average of an aligned kymograph

$$\langle I(x,y) \rangle_y = \frac{1}{m}\sum_{y=1}^{m} I(x,y), \tag{1}$$

where m is the number of rows (time frames) in the kymograph. The reduction in noise can be quantified by the column-wise variance, given by

$$\sigma^2(x) = \frac{1}{m}\sum_{y=1}^{m} [I(x,y) - \langle I(x,y) \rangle_y]^2. \tag{2}$$

To compare WPAlign and the Reisner method [18], these variances were calculated for the 10 representative kymographs in Fig 7, see S1 for experimental details on how these kymographs were obtained. For every column in each of the kymographs, we obtained values $\sigma^2_W(x)$ and $\sigma^2_R(x)$, corresponding to the variances resulting from alignment by the respective

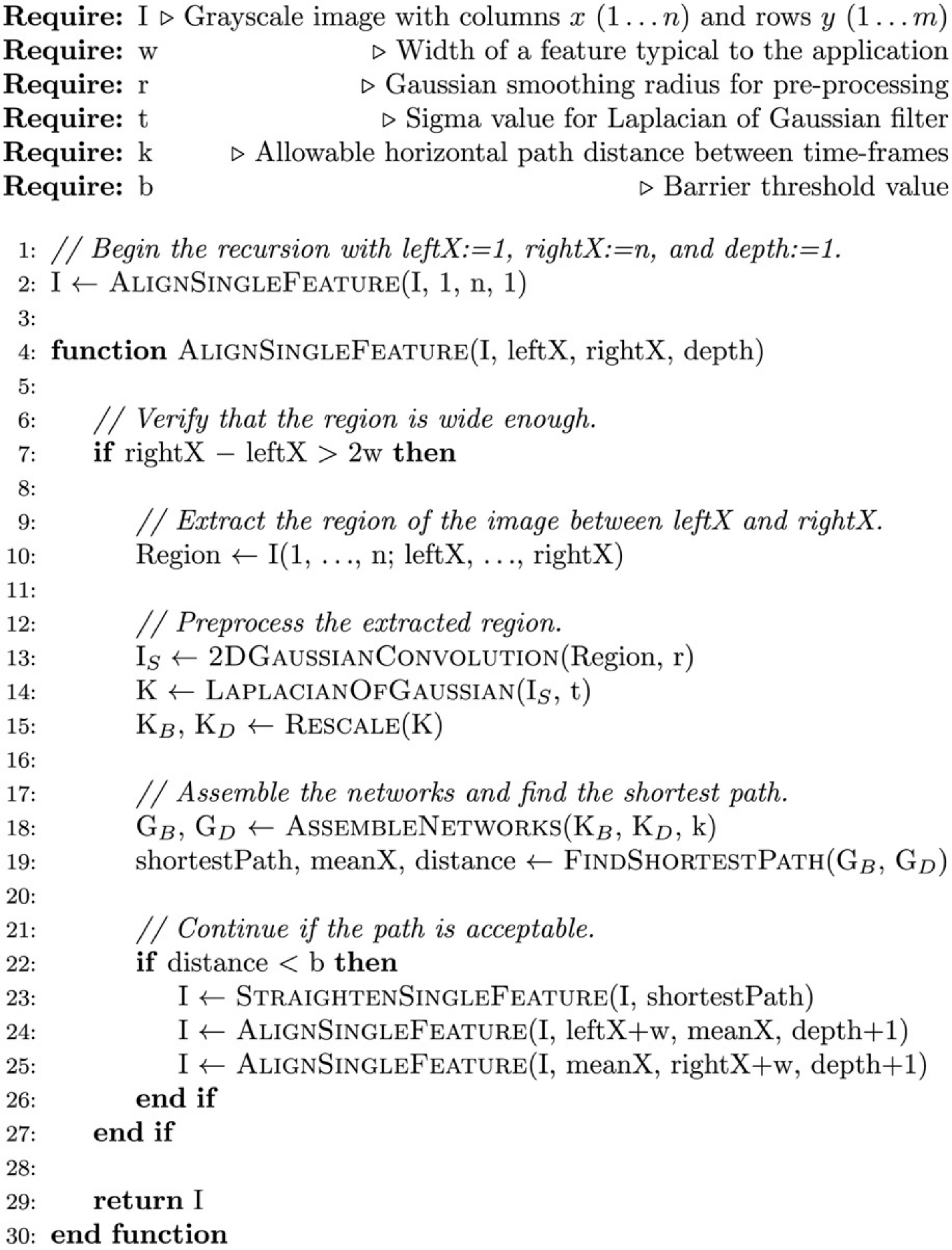

```
Require: I ▷ Grayscale image with columns $x$ $(1 \ldots n)$ and rows $y$ $(1 \ldots m)$
Require: w                      ▷ Width of a feature typical to the application
Require: r                      ▷ Gaussian smoothing radius for pre-processing
Require: t                      ▷ Sigma value for Laplacian of Gaussian filter
Require: k           ▷ Allowable horizontal path distance between time-frames
Require: b                                            ▷ Barrier threshold value

// Begin the recursion with leftX:=1, rightX:=n, and depth:=1.
I ← AlignSingleFeature(I, 1, n, 1)

function AlignSingleFeature(I, leftX, rightX, depth)

    // Verify that the region is wide enough.
    if rightX − leftX > 2w then

        // Extract the region of the image between leftX and rightX.
        Region ← I(1, ..., n; leftX, ..., rightX)

        // Preprocess the extracted region.
        $I_S$ ← 2DGaussianConvolution(Region, r)
        K ← LaplacianOfGaussian($I_S$, t)
        $K_B$, $K_D$ ← Rescale(K)

        // Assemble the networks and find the shortest path.
        $G_B$, $G_D$ ← AssembleNetworks($K_B$, $K_D$, k)
        shortestPath, meanX, distance ← FindShortestPath($G_B$, $G_D$)

        // Continue if the path is acceptable.
        if distance < b then
            I ← StraightenSingleFeature(I, shortestPath)
            I ← AlignSingleFeature(I, leftX+w, meanX, depth+1)
            I ← AlignSingleFeature(I, meanX, rightX+w, depth+1)
        end if
    end if

    return I
end function
```

Fig 6. WPAlign pseudocode. Note that all substeps shown here are available in a variety of standard toolboxes, open-source and otherwise. For our particular implementation, all code was written in Matlab with dependencies in the Image Processing Toolbox and the Bioinformatics Toolbox (which implements the graph data structure and shortest path finding functionality).

doi:10.1371/journal.pone.0121905.g006

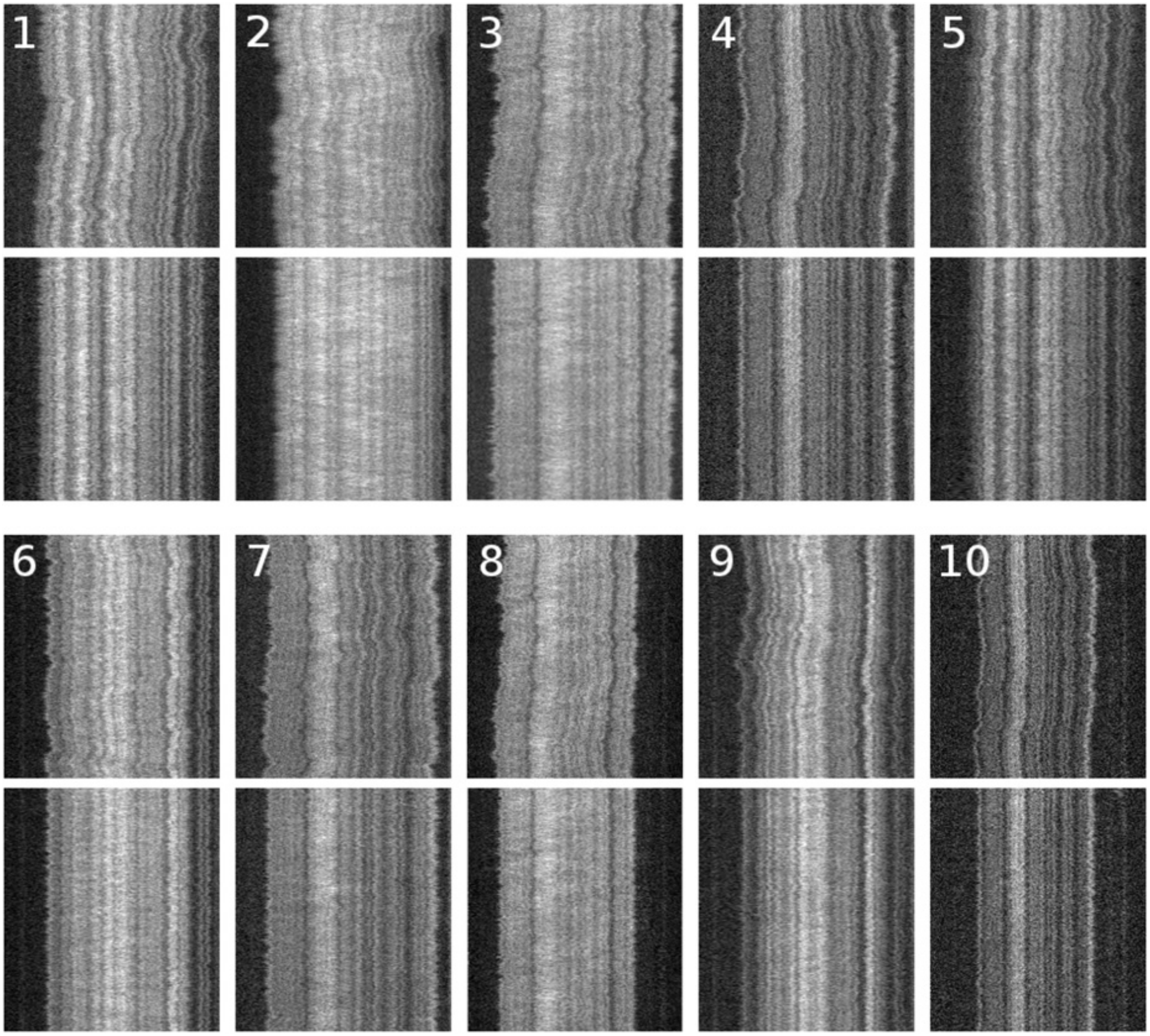

Fig 7. Typical T4GT7 denaturation mapping kymographs, raw and aligned via WPAlign. The numbered kymographs represent the raw data, and the aligned versions are displayed directly below each.

doi:10.1371/journal.pone.0121905.g007

algorithms. Then a distribution of values $\sigma_W^2(x)/\sigma_R^2(x)$ was calculated (see Fig 8). This distribution is normal with mean $\mu = 0.75$, indicating that, for a typical kymograph column, WPAlign reduced variance by 25% when compared to the Reisner method. Thus WPAlign, besides reducing computational costs, reduces kymograph noise and yields an improvement over the Reisner approach.

In addition, we examined how aligned kymograph noise is affected by the length of the time axis (see Fig 9). To do this, we calculated $\langle \sigma^2(x) \rangle$, the mean of the column-wise variances given above, given by

$$\langle \sigma^2(x) \rangle = \frac{1}{n}\sum_{x=1}^{n}\left[\frac{1}{m}\sum_{y=1}^{m}[I(x,y) - \langle I(x,y)\rangle_y]^2\right], \tag{3}$$

for kymographs with time axes ranging from 20 to 200 time frames. From the results we can see that the noise from kymographs aligned via WPAlign is independent of the number of time

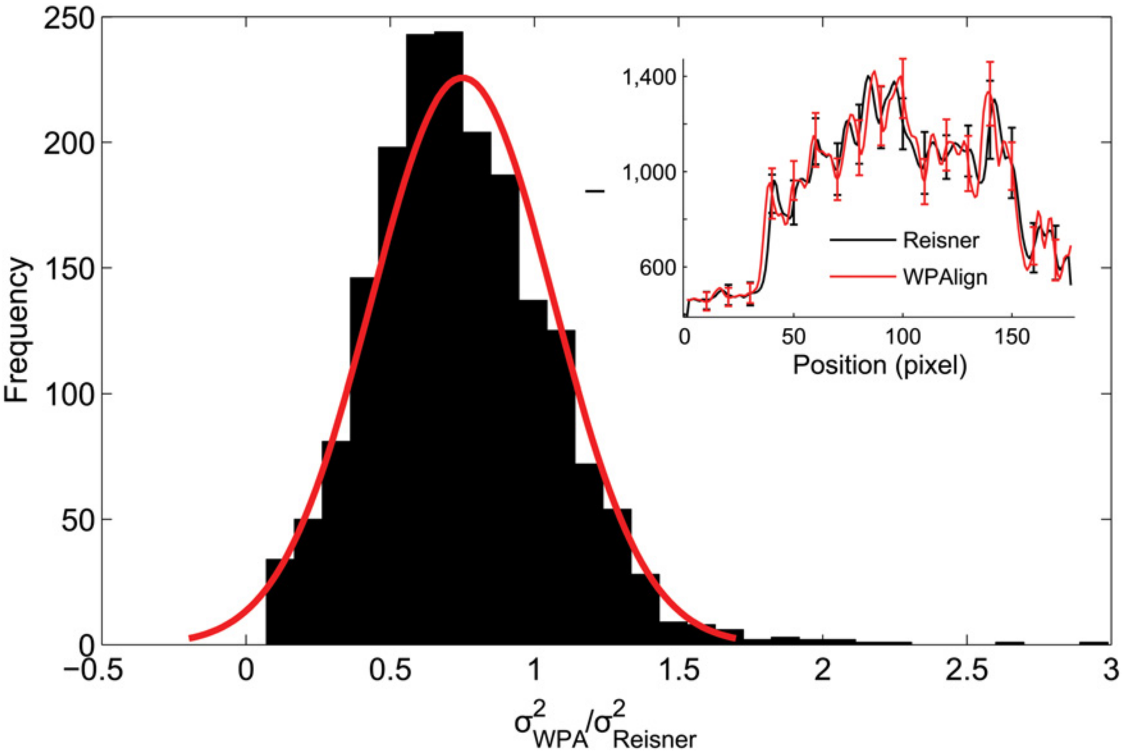

Fig 8. Kymograph noise comparison of WPAlign and the Reisner approach. Column-wise variances were calculated for aligned barcodes using WPAlign ($\sigma^2_W(x)$), and the Reisner approach ($\sigma^2_R(x)$). Here we show the distribution of σ^2_W/σ^2_R. A Gaussian distribution was fit to this data, resulting in a mean of $\mu = 0.75$ (with standard deviation $\sigma = 0.32$). Thus in this particular case, WPAlign reduces variance by 25% compared to the Reisner method. Overall, the fraction of columns such that $\sigma^2_W < \sigma^2_R$ was 80%. (Inset) An example time trace of barcode 6 (see Fig 7) aligned via the WPAlign and Reisner methods. Error bars represent one standard deviation (i.e., σ_W and σ_R).

doi:10.1371/journal.pone.0121905.g008

frames chosen during filming. However, kymographs aligned by the Reisner approach seem to undergo an increase in noise as the number of frames increases, until plateauing at roughly 120 frames.

We present a possible explanation for this result: as the number of time frames increases, the underlying DNA molecule is allowed more time to undergo conformational changes and random diffusive processes, rendering the first and last frames increasingly dissimilar. Thus any template frame chosen by the Reisner method will be increasingly dissimilar from the frames farthest from it in the kymograph. This renders the local stretching factor optimization more prone to becoming stuck in local minima for these “distantly related” frames, introducing noise in the final alignment. WPAlign, on the other hand, avoids this problem as it does not rely on the choice of a single template frame.

Information Score

Before alignment, bright and dark features can stray into adjacent kymograph columns as the DNA molecule undergoes horizontal diffusion. Thus thin features are obscured in the time average, effectively broadening peaks and valleys. As alignments improve, however, features occupy less horizontal space and become more apparent in the final time-trace. Since these features are essential in later performing statistical comparisons with other data, increasing contrast between neighboring features (i.e., increasing feature sharpness) essentially increases the information contained in the time trace.

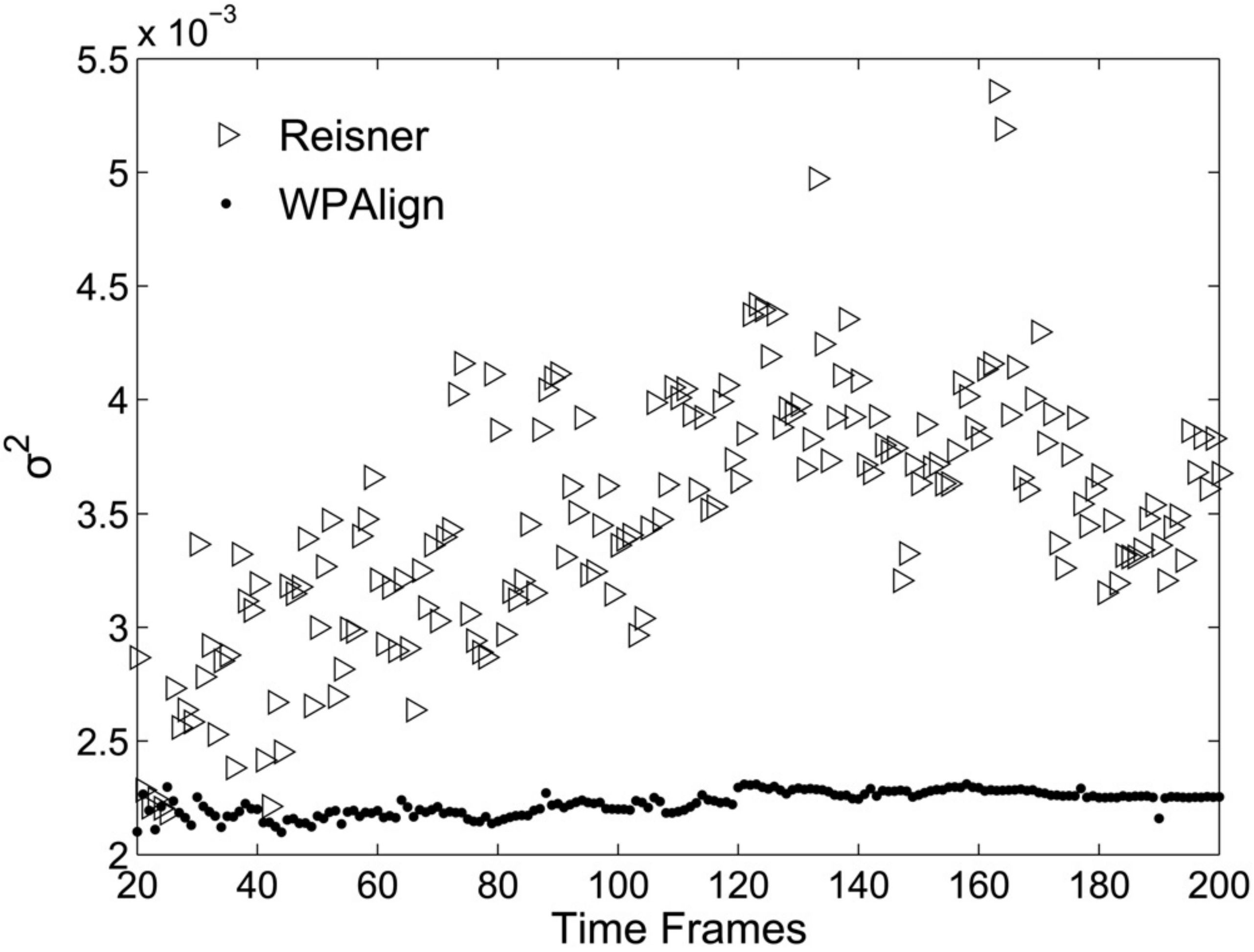

Fig 9. Effect of time axis length on aligned kymograph noise. Kymographs with time axes varying from 20 to 200 time frames in length were aligned by both methods. The resulting column-wise variances $\sigma_R^2(x)$ and $\sigma_W^2(x)$ were calculated as in Fig 8. Here we plot, for each kymograph, the mean of these column variances, i.e., $\langle\sigma_R^2(x)\rangle$ and $\langle\sigma_W^2(x)\rangle$, showing that kymograph noise increases with time axis length for the Reisner method but remains constant for WPAlign.

doi:10.1371/journal.pone.0121905.g009

To quantify this information content of the barcodes we present a new scheme based on the self-information of a random variable [42], see Methods for a comprehensive description. Here in brief, the information score, IS, of a kymograph is given by

$$\mathrm{IS} = \sum_k -\log\left[\frac{1}{\sqrt{2\pi\log(\sigma^2+\chi)}}\exp\left\{-\frac{\log(|\Delta I_k|)^2}{2\log(\sigma^2+\chi)}\right\}\right] \tag{4}$$

where σ^2 represents the noise of the underlying kymograph, $\chi = 1$ is a regularization parameter ensuring that the score remains real-valued for all noise levels, and the ΔI's represent "robust" intensity differences (see S1) between neighboring peaks and valleys. Thus information increases as the difference between neighboring peaks and valleys grows and as the noise of the underlying kymograph decreases. That is, time-traces with sharper, more well-defined local extrema will contain more information than time traces from noisy kymographs with broad extrema.

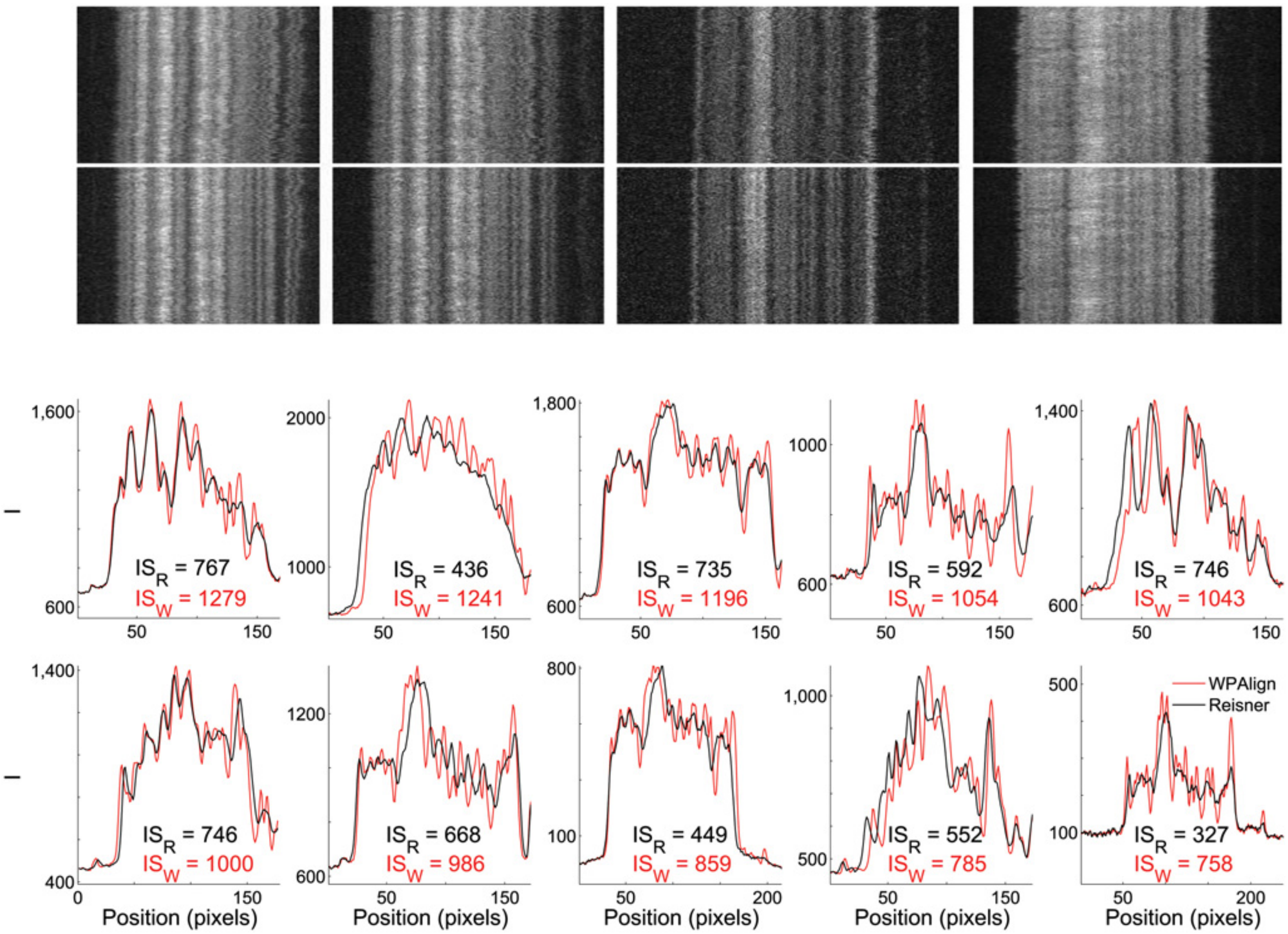

Fig 10. Quality comparison of barcodes aligned via the Reisner approach and WPAlign. (Top) Representative kymographs aligned via the Reisner approach (above) and WPAlign (below). (Bottom) Average intensity traces from kymographs in Fig 7 aligned via WPAlign (red) and the Reisner approach (black). The information score is displayed below each trace for both methods, quantifying the contrast between neighboring features. Notably, $\langle(IS_W - IS_R)/IS_R\rangle = 0.78$, indicating that WPAlign on average produced time-traces with slightly more information than the Reisner method over our sample set. Note that the plots are in the same order as the corresponding kymographs in Fig 7 and are ordered by decreasing IS_W.

doi:10.1371/journal.pone.0121905.g010

Time traces and their corresponding information scores were calculated for the representative kymographs shown in Fig 7 after undergoing alignment by both WPAlign and the Reisner method (see Fig 10). In general, WPAlign produces visually sharper and more well-defined time-traces. Furthermore, the information content is greater for WPAlign in all examples considered. In fact, the average information gain from using WPAlign over the Reisner method on our dataset is roughly 78% (i.e., $\langle(IS_W - IS_R)/IS_R\rangle = 0.78$).

Furthermore, independent of our kymograph alignment technique, this information score can serve as an objective and easily interpretable barcode quality measurement by which barcodes can be compared, providing a basis for experimental optimization. For example, expected barcodes can be calculated from theory for a number of experimental conditions [18], and then experiments can be performed only for barcodes expected to yield the highest information content, saving valuable time and resources for experimentalists. Furthermore, if theory is not available for a particular optical mapping application, the information score can serve as a quality criterion for experimental barcodes by which experimental conditions can be rigorously optimized.

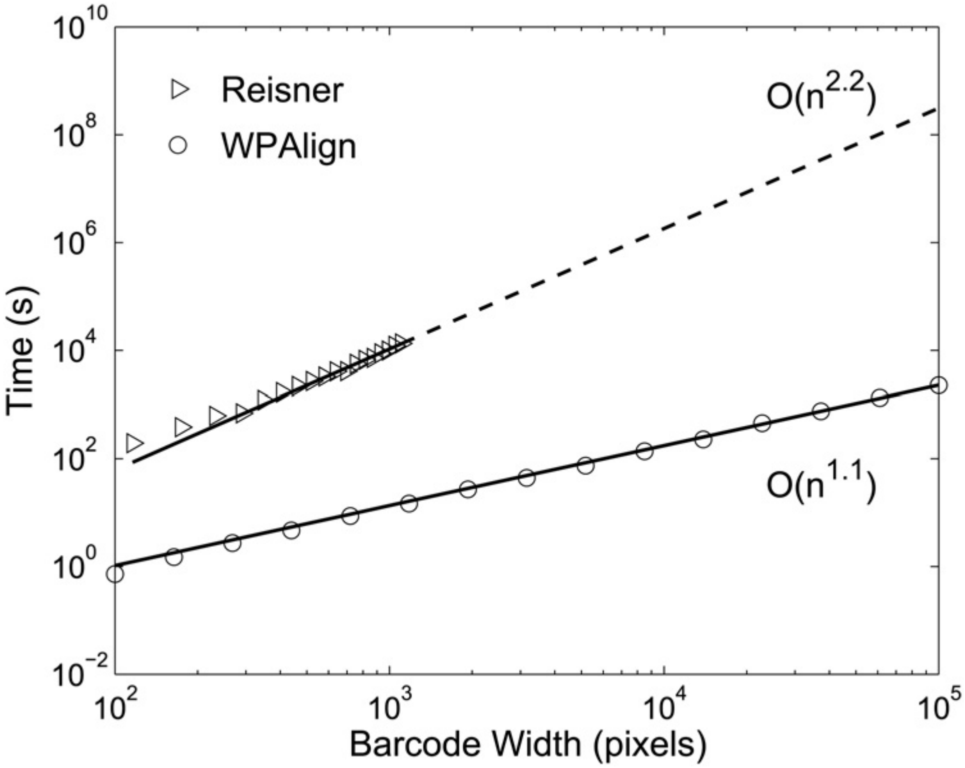

Fig 11. Comparison of time scaling for WPAlign and the Reisner approach. Empirical time scaling results for both techniques on identical kymographs ranging between ∼ 10^2 and ∼ 10^5 pixels in width, where ∼ 10^5 pixels is roughly the length of an intact human genome at current resolutions. Power law curves of the form ax^b were fit to these data (solid lines), yielding $b = 1.1$ for WPAlign, and $b = 2.2$ for the Reisner method. Thus WPAlign exhibits approximately $O(n)$ time scaling with barcode width, while the Reisner method scales approximately with $O(n^2)$. Scaling data beyond ∼ 10^3 pixels was projected for the Reisner approach (dashed line), as alignment times became prohibitive. Simulated kymographs were generated by concatenating experimental T4GT7 kymographs from above.

doi:10.1371/journal.pone.0121905.g011

Computational Time

Empirically, WPAlign exhibits linear scaling with barcode length, n (see Fig 11). This is somewhat intuitive, as the bottleneck of the approach is the shortest path finding algorithm, and this runs in linear time due to the directed and acyclic qualities of our networks. The Reisner approach, on the other hand, scales with $O(n^2)$, rendering it impractical for bacterial barcodes on the order of 1 Mbp or larger (see Fig 11).

Perhaps most importantly, WPAlign was able to successfully align a simulated barcode with length on the order of a full human genome in only 40 minutes. The Reisner approach would require over 10^8 seconds, or roughly 3 years, to perform this task on an identical computer.

Discussion

In this paper we present a new DNA barcode kymograph alignment algorithm which outperforms an existing alternative [18] in computational speed, and for the particular data presented here, also slightly improves on noise reduction properties and information content of the time-averaged barcodes. Indeed, the orders-of-magnitude improvement in computational speed could open the door for high throughput kymograph alignment at the human-genome scale as well as constituting an important step in data analysis for a number of nanofluidic optical mapping techniques, including denaturation mapping [18], fluorocoding [19], competitive binding [20, 21], and enzymatic nicking [23, 24]. By providing a rapid framework for this data analysis, WPAlign can help bring the many applications of optical mapping closer to application, including bacterial strain and species identification, detection of large-scale genomic structural variation, and scaffold building for third generation *de novo* sequencing techniques. Furthermore, the algorithm is easy to implement, as the various substeps involved are available in most standard numerical packages.

Moreover, our feature detection method, suitably modified, may find application in other domains of biological image analysis, such as automated organism tracking [43, 44], or automated study of cellular transport along axons (à la [45–48]), defects in which have been implicated in a number of neurodegenerative diseases, including Alzheimer's Disease, Parkinson's Disease, and Amytrophic Lateral Sclerosis [49, 50].

Finally our information score, motivated as a way to compare the quality of alignments produced by different methods, may find widespread application among the optical mapping community as an easily calculable and interpretable barcode quality criterion by which to optimize experimental conditions.

Supporting Information

S1 Methods. Details on the algorithms presented herein.
(PDF)

Acknowledgments

We thank Karl Åström for helpful discussions on image analysis.

Author Contributions

Conceived and designed the experiments: TA JOT. Performed the experiments: CF JB. Analyzed the data: CN ANN TA. Contributed reagents/materials/analysis tools: CN ANN TA. Wrote the paper: CN ANN JOT TA.

References

1. Aston C, Mishra B, Schwartz DC. Optical mapping and its potential for large-scale sequencing projects. Trends in Biotechnology 1999; 17: 297–302. doi: 10.1016/S0167-7799(99)01326-8 PMID: 10370237
2. Samad A, Huff E, Cai W, Schwartz DC. Optical mapping: a novel, single-molecule approach to genomic analysis. Genome research 1995; 5: 1–4. doi: 10.1101/gr.5.1.1 PMID: 8717049
3. Neely RK, Deen J, Hofkens J. Optical mapping of DNA: Single-molecule-based methods for mapping genomes. Biopolymers 2011; 95: 298–311. doi: 10.1002/bip.21579 PMID: 21207457
4. Das SK, Austin MD, Akana MC, Deshpande P, Cao H, Xiao M. Single molecule linear analysis of DNA in nano-channel labeled with sequence specific fluorescent probes. Nucleic acids research 2010; 38: e177–e177. doi: 10.1093/nar/gkq673 PMID: 20699272
5. Xiao M, Phong A, Ha C, Chan TF, Cai D, Leung L, et al. Rapid DNA mapping by fluorescent single molecule detection. Nucleic acids research 2007; 35: e16–e16. doi: 10.1093/nar/gkl1044 PMID: 17175538
6. Valouev A, Schwartz DC, Zhou S, Waterman MS. An algorithm for assembly of ordered restriction maps from single DNA molecules. Proceedings of the National Academy of Sciences 2006; 103: 15770–15775. doi: 10.1073/pnas.0604040103
7. Valouev A, Li L, Liu YC, Schwartz DC, Yang Y, Zhang Y, et al. Alignment of optical maps. Journal of Computational Biology 2006; 13: 442–462. doi: 10.1089/cmb.2006.13.442 PMID: 16597251
8. Ananiev GE, Goldstein S, Runnheim R, Forrest DK, Zhou S, Potamousis K, et al. Optical mapping discerns genome wide DNA methylation profiles. BMC molecular biology 2008; 9: 68. doi: 10.1186/1471-2199-9-68 PMID: 18667073

9. Jing J, Reed J, Huang J, Hu X, Clarke V, Edington J, et al. Automated high resolution optical mapping using arrayed, fluid-fixed DNA molecules. Proceedings of the National Academy of Sciences 1998; 95: 8046–8051. doi: 10.1073/pnas.95.14.8046

10. Cai W, Jing J, Irvin B, Ohler L, Rose E, Shizuya H, et al. High-resolution restriction maps of bacterial artificial chromosomes constructed by optical mapping. Proceedings of the National Academy of Sciences 1998; 95: 3390–3395. doi: 10.1073/pnas.95.7.3390

11. Conrad DF, Pinto D, Redon R, Feuk L, Gokcumen O, Zhang Y, et al. Origins and functional impact of copy number variation in the human genome. Nature 2009; 464: 704–712. doi: 10.1038/nature08516 PMID: 19812545

12. Redon R, Ishikawa S, Fitch KR, Feuk L, Perry GH, Andrews T D, et al. Global variation in copy number in the human genome. Nature 2006; 444: 444–454. doi: 10.1038/nature05329 PMID: 17122850

13. Shukla SK, Kislow J, Briska A, Henkhaus J, Dykes C. Optical mapping reveals a large genetic inversion between two methicillin-resistant staphylococcus aureus strains. Journal of bacteriology 2009; 191: 5717–5723. doi: 10.1128/JB.00325-09 PMID: 19542272

14. Kotewicz ML, Jackson SA, LeClerc JE, Cebula TA. Optical maps distinguish individual strains of escherichia coli o157: H7. Microbiology 2007; 153: 1720–1733. doi: 10.1099/mic.0.2006/004507-0 PMID: 17526830

15. Zhou S, Kile A, Bechner M, Place M, Kvikstad E, Deng W, et al. Single-molecule approach to bacterial genomic comparisons via optical mapping. Journal of bacteriology 2004; 186: 7773–7782. doi: 10.1128/JB.186.22.7773-7782.2004 PMID: 15516592

16. Zhou S, Deng W, Anantharaman TS, Lim A, Dimalanta ET, Wang J, et al. A whole-genome shotgun optical map of yersinia pestis strain KIM. Applied and environmental microbiology 2002; 68: 6321–6331. doi: 10.1128/AEM.68.12.6321-6331.2002 PMID: 12450857

17. Welch R, Burland V, Plunkett G, Redford P, Roesch P, Rasko D, et al. Extensive mosaic structure revealed by the complete genome sequence of uropathogenic escherichia coli. Proceedings of the National Academy of Sciences 2002; 99: 17020–17024. doi: 10.1073/pnas.252529799

18. Reisner W, Larsen NB, Silahtaroglu A, Kristensen A, Tommerup N, Tegenfeldt JO, et al. Single-molecule denaturation mapping of DNA in nanofluidic channels. Proceedings of the National Academy of Sciences 2010; 107: 13294–13299. doi: 10.1073/pnas.1007081107

19. Neely RK, Dedecker P, Hotta Ji, Urbanavičiūtė G, Klimašauskas S, Hofkens J. DNA fluorocode: a single molecule, optical map of DNA with nanometre resolution. Chemical Science 2010; 1: 453–460. doi: 10.1039/c0sc00277a

20. Nyberg LK, Persson F, Berg J, Bergström J, Fransson E, Olsson L, et al. A single-step competitive binding assay for mapping of single DNA molecules. Biochemical and biophysical research communications 2012; 417: 404–408. doi: 10.1016/j.bbrc.2011.11.128 PMID: 22166208

21. Nilsson AN, Emilsson G, Nyberg LK, Noble C, Stadler LS, Fritzsche J, et al. Competitive binding-based optical DNA mapping for fast identification of bacteria-multi-ligand transfer matrix theory and experimental applications on escherichia coli. Nucleic Acids Research 2014; 42: e118–e118. doi: 10.1093/nar/gku556 PMID: 25013180

22. Lim SF, Karpusenko A, Sakon JJ, Hook JA, Lamar TA, Riehn R. DNA methylation profiling in nanochannels. Biomicrofluidics 2011; 5: 034106. doi: 10.1063/1.3613671

23. Baday M, Cravens A, Hastie A, Kim H, Kudeki DE, et al. Multicolor super-resolution DNA imaging for genetic analysis. Nano letters 2012; 12: 3861–3866. doi: 10.1021/nl302069q PMID: 22698062

24. Das SK, Austin MD, Akana MC, Deshpande P, Cao H, Xiao M. Single molecule linear analysis of DNA in nano-channel labeled with sequence specific fluorescent probes. Nucleic acids research 2010; 38: e177–e177. doi: 10.1093/nar/gkq673 PMID: 20699272

25. Schwartz DC, Li X, Hernandez LI, Ramnarain SP, Huff EJ, et al. Ordered restriction maps of saccharomyces cerevisiae chromosomes constructed by optical mapping. Science 1993; 262: 110–114. doi: 10.1126/science.8211116 PMID: 8211116

26. Meng X, Benson K, Chada K, Huff EJ, Schwartz DC. Optical mapping of lambda bacteriophage clones using restriction endonucleases. Nature Genetics 1995; 9: 432–438. doi: 10.1038/ng0495-432 PMID: 7795651

27. Cai W, Aburatani H, Stanton VP, Housman DE, Wang YK, Schwartz DC. Ordered restriction endonuclease maps of yeast artificial chromosomes created by optical mapping on surfaces. Proceedings of the National Academy of Sciences 1995; 92: 5164–5168. doi: 10.1073/pnas.92.11.5164

28. Schwartz DC, Li X, Hernandez LI, Ramnarain SP, Huff EJ, Wang Y-K. Ordered restriction maps of saccharomyces cerevisiae chromosomes constructed by optical mapping. Science 1993; 262: 110–114. doi: 10.1126/science.8211116 PMID: 8211116

29. Cai W, Aburatani H, Stanton VP, Housman DE, Wang YK, Schwartz DC. Ordered restriction endonuclease maps of yeast artificial chromosomes created by optical mapping on surfaces. Proceedings of the National Academy of Sciences 1995; 92: 5164–5168. doi: 10.1073/pnas.92.11.5164

30. Bensimon A, Simon A, Chiffaudel A, Croquette V, Heslot F, Bensimon D. Alignment and sensitive detection of DNA by a moving interface. Science 1994; 265: 2096–2098. doi: 10.1126/science.7522347 PMID: 7522347

31. Jo K, Dhingra DM, Odijk T, de Pablo JJ, Graham MD, Runnheim R, et al. A single-molecule barcoding system using nanoslits for DNA analysis. Proceedings of the National Academy of Sciences 2007; 104: 2673–2678. doi: 10.1073/pnas.0611151104

32. Douville N, Huh D, Takayama S. DNA linearization through confinement in nanofluidic channels. Analytical and bioanalytical chemistry 2008; 391: 2395–2409. doi: 10.1007/s00216-008-1995-y PMID: 18340435

33. Reisner W, Morton KJ, Riehn R, Wang YM, Yu Z, et al. Statics and dynamics of single DNA molecules confined in nanochannels. Physical Review Letters 2005; 94: 196101. doi: 10.1103/PhysRevLett.94.196101 PMID: 16090189

34. Reisner W, Pedersen JN, Austin RH. DNA confinement in nanochannels: physics and biological applications. Reports on Progress in Physics 2012; 75: 106601. doi: 10.1088/0034-4885/75/10/106601 PMID: 22975868

35. Tegenfeldt JO, Prinz C, Cao H, Chou S, Reisner WW, Riehn R, et al. The dynamics of genomic-length DNA molecules in 100-nm channels. Proceedings of the National Academy of Sciences of the United States of America 2004; 101: 10979–10983. doi: 10.1073/pnas.0403849101 PMID: 15252203

36. Persson F, Tegenfeldt JO. DNA in nanochannels-directly visualizing genomic information. Chemical Society Reviews 2010; 39: 985–999. doi: 10.1039/b912918a PMID: 20179820

37. Marie R, Pedersen JN, Bauer DL, Rasmussen KH, Yusuf M, Volpi E, et al. Integrated view of genome structure and sequence of a single DNA molecule in a nanofluidic device. Proceedings of the National Academy of Sciences 2013; 110: 4893–4898. doi: 10.1073/pnas.1214570110

38. Hebert PDN, Cywinska A, Ball SL. Biological identifications through DNA barcodes, Proceedings of the Royal Society B 2003; 270, 313. doi: 10.1098/rspb.2002.2218 PMID: 12614582

39. Reisner W, Morton KJ, Riehn R, Wang YM, Yu Z, Rosen M, et al. Statics and dynamics of single DNA molecules confined in nanochannels. Phys. Rev. Lett. 2005; 94: 196101. doi: 10.1103/PhysRevLett.94.196101 PMID: 16090189

40. De Gennes PG, Scaling concepts in polymer physics. Cornell university press, 1979.

41. Leiserson CE, Rivest RL, Stein C, Cormen TH. Introduction to algorithms. The MIT press, 2001.

42. Cover TM, Thomas JA. Entropy, relative entropy and mutual information. Elements of Information Theory 1991: 12–49. doi: 10.1002/0471200611.ch2

43. Tsibidis GD, Tavernarakis N. Nemo: a computational tool for analyzing nematode locomotion. BMC neuroscience (2007); 8: 86. doi: 10.1186/1471-2202-8-86 PMID: 17941975

44. Huang KM, Cosman P, Schafer WR. Automated detection and analysis of foraging behavior in c. elegans. In: Image Analysis and Interpretation, 2008. SSIAI 2008. IEEE Southwest Symposium on. IEEE, 2008: 29–32.

45. Chetta J, Shah SB. A novel algorithm to generate kymographs from dynamic axons for the quantitative analysis of axonal transport. Journal of neuroscience methods 2011; 199: 230–240. doi: 10.1016/j.jneumeth.2011.05.013 PMID: 21620890

46. Obashi K, Okabe S. Regulation of mitochondrial dynamics and distribution by synapse position and neuronal activity in the axon. European Journal of Neuroscience 2013; 38: 2350–2363. doi: 10.1111/ejn.12263 PMID: 23725294

47. Zhou HM, Brust-Mascher I, Scholey JM. Direct visualization of the movement of the monomeric axonal transport motor unc-104 along neuronal processes in livingcaenorhabditis elegans. The Journal of Neuroscience 2001; 21: 3749–3755. PMID: 11356862

48. Miller KE, Sheetz MP. Axonal mitochondrial transport and potential are correlated. Journal of Cell Science 2004; 117: 2791–2804. doi: 10.1242/jcs.01130 PMID: 15150321

49. Chevalier-Larsen E, Holzbaur EL. Axonal transport and neurodegenerative disease. Biochimica et Biophysica Acta (BBA)-Molecular Basis of Disease 2006; 1762: 1094–1108. doi: 10.1016/j.bbadis.2006.04.002

50. Haghnia M, Cavalli V, Shah SB, Schimmelpfeng K, Brusch R, Yang G, et al. Dynactin is required for coordinated bidirectional motility, but not for dynein membrane attachment. Molecular biology of the cell 2007; 18: 2081–2089. doi: 10.1091/mbc.E06-08-0695 PMID: 17360970